Nano Research

Open Access

Research Article

In-situ synthesis of $Ni_3Sn_2S_2$ heterojunction to boost the polarization and electromagnetic performance of FeCoCrNiAl high-entropy alloy

Haipeng Xiang[1], Yi Liu[1] ✉, Xiaohui Zhao[1] ✉, Qiang Wang[1], Wanxiang Zheng[3] ✉, Lei Zhang[3], Xiaolei Su[1] ✉, and Chuanyin Xiong[2] ✉

[1] *School of Materials Science & Engineering, Xi'an Polytechnic University, Xi'an 710048, China*
[2] *College of Bioresources Chemistry and Materials Engineering, Shaanxi University of Science and Technology, Xi'an 710021, China*
[3] *Department of Urology, Xijing Hospital, Air Force Medical University, Xi'an 710032, China*

Cite this article: *Nano Research*, **2026**, *19*, 94908494. https://doi.org/10.26599/NR.2026.94908494

ABSTRACT: This study utilizes FeCoCrNiAl itself as the Ni source to grow the Shandite phase $Ni_3Sn_2S_2$ *in situ* on its surface. By constructing $Ni_3Sn_2S_2$@FeCoCrNiAl with heterogeneous interfaces and continuous nanocoating, further modulated interfacial charge transfer and d-p hybridization while integrating the thermal conduction network. This approach simultaneously enhanced microwave absorption and thermal conductivity, balancing the opposing effects of interfacial phenomena on phonon heat transfer and microwave absorption. Multi-scale characterization techniques confirm the formation of crystalline phases and the achievement of dense, uniform coating, with increasing content leading to more uniform and dense coatings. The synergistic effect between dielectric loss based on $Ni_3Sn_2S_2$ and magnetic loss from high-entropy alloys achieves a minimum reflection loss (RL_{min}) of −44.26 dB. After introducing a frequency-selective surface (FSS), the thickness is optimized to 1.4 mm, further reducing RL_{min} to −60.47 dB. Regarding thermal conductivity, the 30 wt.% silicone rubber composite sample achieved a ΔT = 104.3 °C temperature rise within 8 s. Density functional theory (DFT) calculations reveal that transition metal d orbitals (Fe/Co/Ni, including Ni at the $Ni_3Sn_2S_2$ side) overlap with S-3p orbitals at the interface, forming d-p hybridization and creating a more continuous conductive state. The plane-averaged differential charge density reveals an interfacial dipole layer of approximately 1.2 Å (peaking at 6.53 and 7.71 Å), indicating electron migration from a high-entropy alloy (HEA) to $Ni_3Sn_2S_2$. This leads to interfacial polarization and enhanced dielectric loss. The afore mentioned electronic structural evidence aligns with macroscopic testing, providing new ideas for developing multifunctional microwave absorption and thermal conductivity materials.

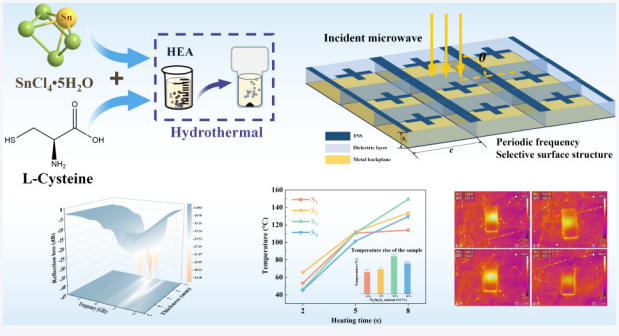

KEYWORDS: $Ni_3Sn_2S_2$@FeCoCrNiAl heterostructure, microwave-absorbing silicone rubber, density functional theory (DFT), frequency-selective surface (FSS)

1 Introduction

With the rapid development of wireless communication and radar technology, electromagnetic interference issues have become increasingly severe, thus placing higher demands on microwave absorption materials in terms of electromagnetic shielding, radar cross-section (RCS) control [1–5], and heat dissipation for electronic devices. Ideal microwave absorption materials must possess efficient absorption capabilities and maintain excellent thermal conductivity [6–9]. To meet the application requirements for stable operation under high-frequency, high-power, and complex multi-scenario environments, research on microwave absorption materials is increasingly focusing on the development of "lightweight, thin, high-performance, and wide-bandwidth" materials, making it a hot topic in the field of functional materials [10–14].

In current domestic and international research, common microwave absorption materials primarily include ferromagnetic

Received: December 18, 2025; **Revised:** January 20, 2026
Accepted: January 25, 2026

✉Address correspondence to Yi Liu, yiliu1021@163.com; Xiaohui Zhao, xhuizhao@xpu.edu.cn; Wanxiang Zheng, zhengwx11@163.com; Xiaolei Su, suxiaolei@xpu.edu.cn; Chuanyin Xiong, xiongchuanyin@126.com

materials (such as Fe_3O_4, FeSiAl), conductive carbon materials (such as graphene, carbon nanotubes) [15–18], and semiconductor-type sulfides such as SnS_2 and MoS_2 [19–22]. Combining these materials with polymer matrices such as silicone rubber and polyimide establishes a synergistic mechanism between dielectric and magnetic loss to enhance absorption performance [23–28]. Some studies have also employed surface modification techniques such as doping and heterostructure construction to regulate their dielectric constant and complex magnetic permeability [29–31], thereby optimizing impedance matching [32–34]. However, such systems are often single-component or simple composite structures, making it difficult to form stable multi-scale synergistic networks. Additionally, traditional microwave absorption materials generally have poor thermal conductivity, leading to heat accumulation under intense microwave exposure and degraded performance [35]. High-entropy alloys (HEAs) exhibit excellent thermal stability, mechanical properties [36, 37], and magnetic loss capabilities due to their multi-component synergistic effects and solid solution structures, making them suitable as magnetic loss carriers [38]. However, their dielectric loss capabilities are insufficient, limiting their comprehensive performance as standalone absorbers. Therefore, introducing high-conductivity materials with strong dielectric responses to construct interface polarization and conductive loss pathways has become necessary. $Ni_3Sn_2S_2$ is a ternary transition metal chalcogenide with an $R\bar{3}m$ space group Shandite structure. In its crystal structure [39], Ni atoms arrange in a two-dimensional (2D) Kagome metallic lattice [40], exhibiting good conductivity and multiple polarization centers, demonstrating excellent dielectric loss properties. Currently, domestic and international research on $Ni_3Sn_2S_2$ and Shandite-structured materials primarily focuses on their physicochemical properties and energy applications [41, 42], with widespread use in electrode materials and catalytic systems. Studies indicate that their interaction with carbon networks and other heterogeneous interfaces can promote electron migration and interfacial polarization, which is expected to expand their application potential in the field of microwave absorption materials.

Combining $Ni_3Sn_2S_2$ with a high-entropy alloy of FeCoCrNiAl forms a dielectric–magnetic two-component system. The heterointerface between the two enhances polarization relaxation and multiple scattering, while introducing a magnetoelectric synergy loss mechanism, significantly improving impedance matching and reducing reflection loss [43, 44]. Additionally, the continuous $Ni_3Sn_2S_2$ nanocoating can establish an efficient thermal conduction network on the alloy surface, effectively compensating for interfacial thermal resistance, thereby achieving the dual-function integration of microwave absorption and thermal diffusion. This composite system provides a new approach for developing high-performance, multifunctional microwave absorption and thermally conductive materials.

This study proposes a novel system that utilizes FeCoCrNiAl high-entropy alloy as the Ni source and introduces a reducing sulfur source to construct $Ni_3Sn_2S_2$ on the alloy surface via *in situ* hydrothermal synthesis, thereby obtaining $Ni_3Sn_2S_2$@FeCoCrNiAl alloy powder. This structure combines the layered high conductivity of $Ni_3Sn_2S_2$ with the multi-element synergistic effects of high-entropy alloys. The performance of the composite powder in terms of microwave absorption, thermal conductivity, and RCS is systematically investigated.

2 Experimental

The preparation process and mechanism of $Ni_3Sn_2S_2$@FeCoCrNiAl composite powder are shown in Fig. 1(a). The main processes include alkali washing pretreatment and *in situ* hydrothermal treatment. Samples S1–S4 correspond to contents of 10%–40%. The specific preparation process is as follows:

2.1 Preparation of $Ni_3Sn_2S_2$@FeCoCrNiAl composite powder

The 4N-purity FeCoCrNiAl high-entropy alloy powder was placed in a 1.5 mol/L NaOH solution, sonicated for 30 min, and allowed to stand for 1 h. Subsequently, sequential washing with deionized water and neutral alcohol, and HF-NaF roughening treatment were performed to enhance the surface activity of the powder. The pretreated powder was dispersed in deionized water containing 3.5 g/L poly(vinylpyrrolidone) (PVP), and 0.20 mol/L $SnCl_4{\cdot}5H_2O$, 0.002 mol/L citric acid, and an equimolar amount of L-cysteine were added. The mixture was subjected to hydrothermal reaction at 150 °C for 12 h. After cooling, the product was washed multiple times with water and ethanol and vacuum-dried to obtain FeCoCrNiAl composite powder uniformly coated with $Ni_3Sn_2S_2$.

2.2 Preparation of $Ni_3Sn_2S_2$@FeCoCrNiAl silicone rubber

The prepared $Ni_3Sn_2S_2$@FeCoCrNiAl composite powder was uniformly dispersed in 0.6875 g of room-temperature vulcanizing silicone rubber, with 0.0688 g of fumed silica added as a reinforcing filler, and stirred until uniform and transparent. Then, 0.0138 g of methyl silicone oil was added for dilution, followed by 0.0138 g of hydroxy silicone oil and 0.0275 g of ethyl silicate as crosslinking agents. Finally, 0.0750 g of dibutyl tin dilaurate was added to catalyze the curing reaction. After thorough mixing at room temperature, the mixture was left to cure. After demolding, samples were obtained to test subsequent electromagnetic and thermal conductivity properties.

2.3 Density functional theory (DFT) calculation

In the first-principles calculations, to represent the disordered solid solution of the FeCoCrNiAl high-entropy alloy, a 40-atom SQS supercell was generated with ATAT's mcsqs. After verification and format conversion via VASPKIT, the data was imported into Materials Studio (CASTEP). The computational task was set as geometric optimization, with exchange-correlation interactions modeled using PBEsol within the GGA framework. The pseudopotential employed the OTFG ultra-soft library, with a plane-wave cutoff energy of 400 eV. Spins were treated as collinear with "use formal spin as initial" enabled; DFT+U and spin-orbit coupling were not employed. The system was modeled as metal-occupied (metal option) with zero net charge. The k-point grid was automatically generated by VASPKIT with reciprocal space resolution, and the mesh and convergence threshold were determined via convergence tests. For constructing the $Ni_3Sn_2S_2$@FeCoCrNiAl heterostructure, in-plane collinear matching was employed with sufficient vacuum and dipole corrections introduced along the normal direction. After full relaxation of the structure, calculations for band structure/density of states (DOS) and differential charge density were performed on a denser k-space grid within the same exchange-correlation framework.

2.4 Characterization

The powder's crystal structure and phase composition were determined using X-ray diffraction (XRD), and the formation of $Ni_3Sn_2S_2$ was confirmed using PDF cards. SEM was used to observe

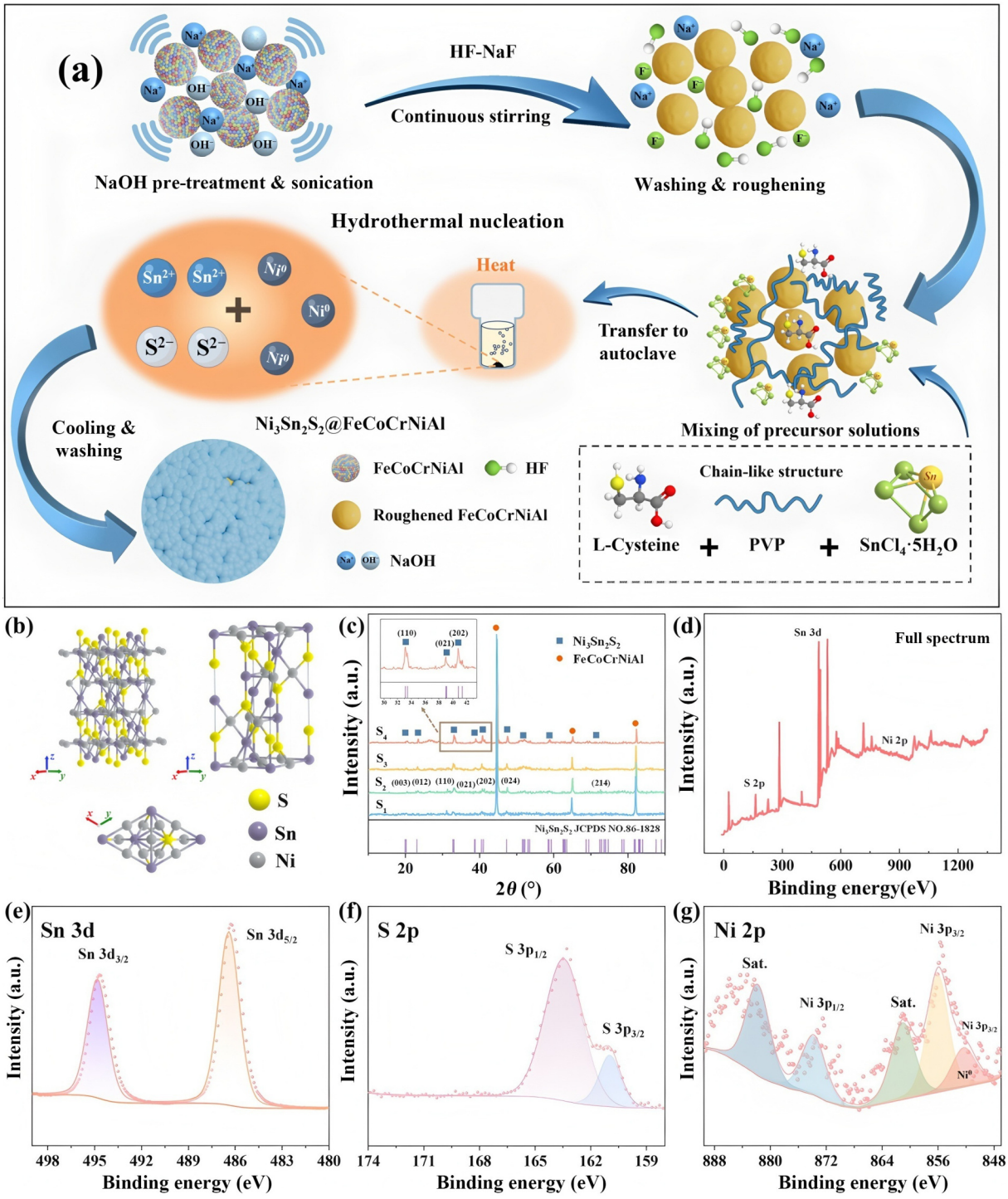

Figure 1 (a) Schematic diagram of the preparation of $Ni_3Sn_2S_2$@FeCoCrNiAl composite powder. (b) Schematic of the crystalline structure of the Kagome-lattice $Ni_3Sn_2S_2$. (c) S1–S4 XRD patterns of $Ni_3Sn_2S_2$@FeCoCrNiAl. (d)–(g) XPS spectra of $Ni_3Sn_2S_2$@FeCoCrNiAl.

the surface morphology and coating distribution of the composite powder, while high-resolution TEM further revealed the coating's nanostructure and crystal plane information. X-ray photoelectron spectroscopy (XPS) analysis was used to analyze the valence state and chemical bonding state of the elements, verifying the existence forms of Ni, Sn, and S in $Ni_3Sn_2S_2$. A vector network analyzer was used to test the material's complex dielectric constant and magnetic permeability, evaluating its electromagnetic parameters. Infrared thermal imaging was employed to assess its thermal conductivity, and simulation software was used to model and calculate RCS, comprehensively evaluating the material's microwave absorption, thermal conductivity, and stealth performance.

3 Results and discussion

XRD analysis was performed on composite powders of $Ni_3Sn_2S_2$@FeCoCrNiAl with different $Ni_3Sn_2S_2$ contents (S1–S4). $Ni_3Sn_2S_2$ belongs to the typical $R\bar{3}m$ space group Shandite structure

(Fig. 1(b)), where the square markers indicate the characteristic peaks of $Ni_3Sn_2S_2$, and the dot markers indicate the high-entropy alloy peaks of FeCoCrNiAl. These correspond to the (003), (012), (110), (021), (202), (024), and (214) crystal planes of $Ni_3Sn_2S_2$ (Fig. 1(c)). XRD results show that as the $Ni_3Sn_2S_2$ content increases, the intensity of the diffraction peaks gradually increases in the S1–S4. In the S4, the $Ni_3Sn_2S_2$ diffraction peaks are sharper and significantly stronger, indicating complete crystal growth and high crystallinity. The $Ni_3Sn_2S_2$ diffraction peaks observed in all samples correspond to the standard PDF card (JCPDS No. 86-1828), with no prominent impurity peaks, indicating that $Ni_3Sn_2S_2$ has high purity and has been successfully in situ generated on the surface of the FeCoCrNiAl alloy.

Further analysis of the chemical valence states and bonding environments of each element in the $Ni_3Sn_2S_2$@FeCoCrNiAl composite powder was conducted using XPS. The spectrum of the Sn element (Fig. 1(e)) exhibits two distinct split peaks at 486.40 (Sn $3d_{5/2}$) and 494.81 eV (Sn $3d_{3/2}$), with a binding energy difference of 8.41 eV, consistent with the characteristic features of Sn^{2+} in metal sulfides [45–48]. The peak shapes are symmetrical, and no shoulder peaks or additional peak positions on the high-binding-energy side are observed. The results indicate that Sn exists stably in the +2 oxidation state in the sample, and no significant surface oxidation or formation of Sn–O secondary phases is observed. In the corresponding S 2p spectrum, two peaks are observed at 161.10 (S $2p_{3/2}$) and 163.20 eV (S $2p_{1/2}$), with the area ratio of the two peaks being approximately 2:1, consistent with the ratio of the split characteristic peaks of the S 2p orbitals. This indicates that in $Ni_3Sn_2S_2$, as shown in Fig. 1(f), S atoms primarily exist in the S^{2-} form, and no high-binding-energy peaks were observed in the 168–170 eV range, further ruling out the presence of surface sulfur oxides. In the Ni spectrum (Fig. 1(g)), the XPS spectrum of Ni 2p shows a characteristic peak for metallic Ni at 852.3 eV, along with distinct Ni $2p_{3/2}$ and Ni $2p_{1/2}$ peaks at 856.0 and 873.8 eV, respectively, along with their corresponding satellite peaks (861.0 and 881.8 eV) [49–52], indicating that Ni exists in $Ni_3Sn_2S_2$ in a partially reduced state close to zero valence and contains Ni^{2+}. Based on literature and precursor reaction mechanism analysis, Ni^{2+} is reduced to zero-valent Ni^0 under hydrothermal conditions by the reducing component L-cysteine, then diffuses into the SnS lattice, reacting with Sn and S to form $Ni_3Sn_2S_2$. This process aligns with the bonding characteristics of Ni atoms in the layered Kagome metal network within the Shandite structure. In summary, the XPS analysis results reveal the bonding state of $Ni_3Sn_2S_2$ in the material, confirming it as a typical ternary tin-sulfur compound with a Shandite structure, with no other peaks observed. This is consistent with the XRD and morphological characterization structures, further indicating that the prepared $Ni_3Sn_2S_2$ exhibits excellent purity and chemical homogeneity.

Based on the results from XPS, TEM, and other characterization techniques mentioned earlier, the formation mechanism of $Ni_3Sn_2S_2$ was further analyzed. $Ni_3Sn_2S_2$ belongs to the Shandite type structure of the $R\bar{3}m$ space group, with Ni atoms arranged in a 2D Kagome hexagonal metallic lattice within the crystal. Under hydrothermal conditions, $SnCl_4{\cdot}5H_2O$ releases Sn^{4+} through hydrolysis during the initial reaction stage. L-cysteine acts as a reducing ligand, and during heating, its sulfhydryl group (–SH) undergoes cleavage, releasing electrons and S^{2-}, thereby reducing Sn^{4+} to Sn^{2+} and further forming SnS precursor crystal nuclei. This process effectively regulates the valence state and release rate of tin ions.

Meanwhile, the FeCoCrNiAl high-entropy alloy treated with alkali washing undergoes ionic corrosion of Ni on its surface, resulting in the dissolution of Ni^{2+} in the acidic environment provided by HCl generated from the hydrolysis of $SnCl_4$. Subsequently, the released –SH reduces Ni^{2+} *in situ* to highly active Ni^0. This *in situ*-generated Ni^0 diffuses and incorporates into the SnS lattice, reacting with Sn^{2+} and S^{2-} to form $Ni_3Sn_2S_2$ crystals with a Shandite-type structure. Notably, PVP acts as a structural regulator by adsorbing its long-chain molecules onto the crystal surface, controlling the nucleation orientation and growth rate of the crystals, providing effective steric hindrance, inhibiting Ni^0 aggregation, and maintaining high reactivity, thereby achieving continuous nucleation and uniform coating of $Ni_3Sn_2S_2$. The ionic reaction is as follows (Eqs. (1)–(4))

$$C_3H_7NO_2S \rightarrow \text{cystine} + 2H^+ + 2e^- + S^{2-} \quad (1)$$

$$Sn^{4+} + \text{L-cysteine} \rightleftharpoons [Sn(Cys)]^{2+} \quad (2)$$

$$Ni^{2+} + 2e^- \rightarrow Ni^0 \quad (3)$$

$$3Ni^0 + 2SnS \rightarrow Ni_3Sn_2S_2 \quad (4)$$

To further analyze the *in-situ* growth extent and coating morphology characteristics of $Ni_3Sn_2S_2$ on the surface of FeCoCrNiAl high-entropy alloys as the content increases, $Ni_3Sn_2S_2$@FeCoCrNiAl composite powders were characterized using scanning electron microscopy (SEM) and transmission electron microscopy (TEM) (Fig. 2). From the SEM images, it can be observed that as the $Ni_3Sn_2S_2$ content increases, the spherical FeCoCrNiAl particles gradually form a more compact granular structure on the surface, resulting in significant changes in the surface structure of the composite particles. In the low-content S1 (Fig. 2(a)), the surface of the FeCoCrNiAl particles remains relatively smooth, with only a few scattered overlying particles visible, indicating that $Ni_3Sn_2S_2$ has not yet achieved continuous coating. In S2 to S4 (Figs. 2(b)–2(d)), the surface of the FeCoCrNiAl spherical particles is gradually covered by a dense granular outer layer structure, indicating that the coating of $Ni_3Sn_2S_2$ is approaching completeness. Particularly in the S4 shown in Fig. 2(d), the particle surfaces exhibit a rough outer layer composed of fine particles, whose morphology is characterized by many aggregated nanoparticle clusters in the local magnification image (Fig. 2(d_1)). To verify the elemental composition of this rough layer, an EDS surface scan was performed on the S3 (Fig. 2(e)). The results show that the surface region exhibits significant enrichment of Ni, Sn, and S signals. At the same time, Fe, Co, Cr, and Al elements of the FeCoCrNiAl alloy are weakly distributed in the surface layer, suggesting they are primarily retained within the particles. This elemental distribution characteristic indicates that Ni elements in the alloy selectively leach out during the reaction process and participate in forming the outer layer products. Under the combined action of Sn and S sources, $Ni_3Sn_2S_2$ is formed *in situ* on the surface, verifying that the outer layer structure originates from the active components of the alloy itself, consistent with the *in-situ* growth and construction scenario mentioned earlier.

The TEM images of $Ni_3Sn_2S_2$@FeCoCrNiAl are shown in Figs. 2(f)–2(h). As shown in Fig. 2(f), the surface of the high-entropy alloy particles is covered by a uniform and dense

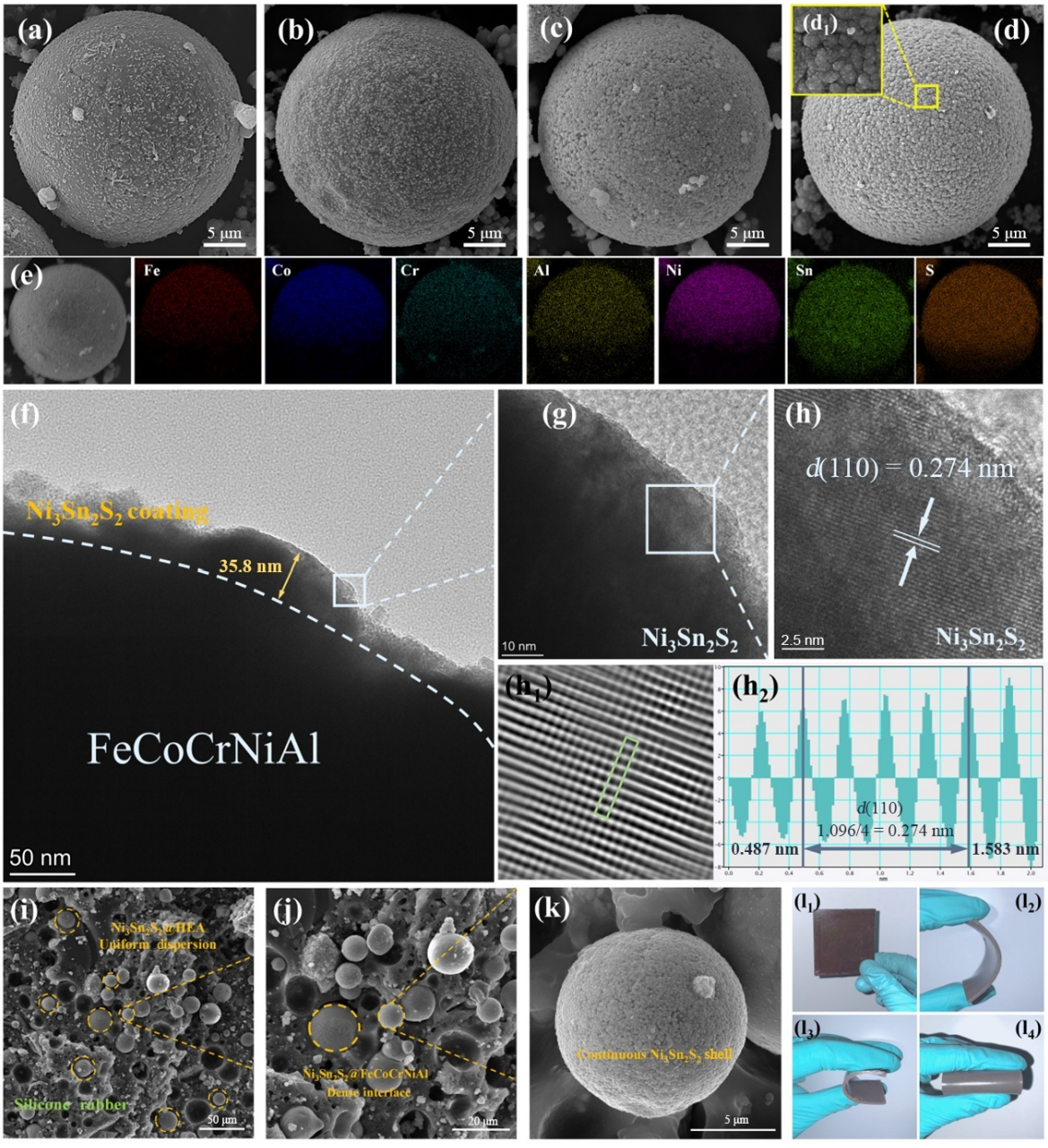

Figure 2 Characterization of the $Ni_3Sn_2S_2$@FeCoCrNiAl composite. (a)–(d) SEM images of $Ni_3Sn_2S_2$@FeCoCrNiAl composite powder. (e) EDS mapping of $Ni_3Sn_2S_2$@FeCoCrNiAl composite powder. (f)–(h) TEM images of $Ni_3Sn_2S_2$@FeCoCrNiAl composite powder. (i)–(k) Cross-sectional SEM images of $Ni_3Sn_2S_2$@FeCoCrNiAl–silicone rubber. (l_1)–(l_4) Flexible $Ni_3Sn_2S_2$@FeCoCrNiAl silicone rubber optical photograph.

nanostructured coating layer with a thickness of approximately several dozen nanometers. Figure 2(g) shows a clear interface and smooth transition between the coating layer and the FeCoCrNiAl substrate, with no pores, delamination, or other structural defects, indicating good interface adhesion. Further high-resolution TEM images (Fig. 2(h)) reveal clear lattice fringes. The interplanar spacing was measured to be 0.274 nm by Fourier transform analysis (Fig. 2(h_1)–(h_2)), consistent with the (110) crystal plane of $Ni_3Sn_2S_2$ in JCPDS card No. 86-1828, further confirming that the coating layer is a $Ni_3Sn_2S_2$ crystal with a Shandite-type structure. This demonstrates the successful *in situ* synthesis of $Ni_3Sn_2S_2$ on the surface of the high entropy alloy FeCoCrNiAl.

SEM further confirms excellent compatibility between $Ni_3Sn_2S_2$@FeCoCrNiAl and the silicone rubber, with no obvious interfacial voids (Figs. 2(i)–2(k)). The $Ni_3Sn_2S_2$@FeCoCrNiAl particles are uniformly dispersed in the silicone rubber, with almost no agglomeration or sedimentation (Fig. 2(i)). This dense encapsulation functions as an impermeable physical barrier, effectively isolating the sensitive sulfide phase from oxygen and thereby preventing oxidation during high-temperature operation. At higher magnification, the particles adhering to the silicone rubber surface with no discernible gaps at the interface, indicating strong interfacial adhesion and no signs of delamination (Fig. 2(j)). This reduces reflections caused by air voids, improves impedance matching, leading to stronger reflection loss. Meanwhile, the continuous and seamless interfaces help form continuous thermal pathways, lower the interfacial thermal resistance, effectively enhancing thermal conductivity. During mixing and curing, the

core–shell structure remains intact; the $Ni_3Sn_2S_2$ coating uniformly encapsulates the FeCoCrNiAl core, with no shell delamination or cracking observed (Fig. 2(k)). Figure 2(l_1)–2(l_4) show optical photographs of $Ni_3Sn_2S_2$@FeCoCrNiAl silicone rubber. It can be observed that the material can be repeatedly bent to a small radius of curvature at room temperature without visible cracking or interfacial delamination, demonstrating excellent flexibility and processability.

Figure 3 shows the variation trends of the complex dielectric constant $\varepsilon_r = (\varepsilon' - j\varepsilon'')$and complex magnetic permeability $\mu_r = (\mu' - j\mu'')$ of the $Ni_3Sn_2S_2$@FeCoCrNiAl composite material under different $Ni_3Sn_2S_2$ content conditions [53]. ε' reflects the material's energy storage capacity and is related to its ability to generate polarization under the influence of an electromagnetic field. ε'' determines the material′ s ability to dissipate energy from electromagnetic waves. In Fig. 3(a), the real part of the dielectric constant ε' shows a slight decrease overall as the $Ni_3Sn_2S_2$ content increases. When a periodic electromagnetic field is applied to the

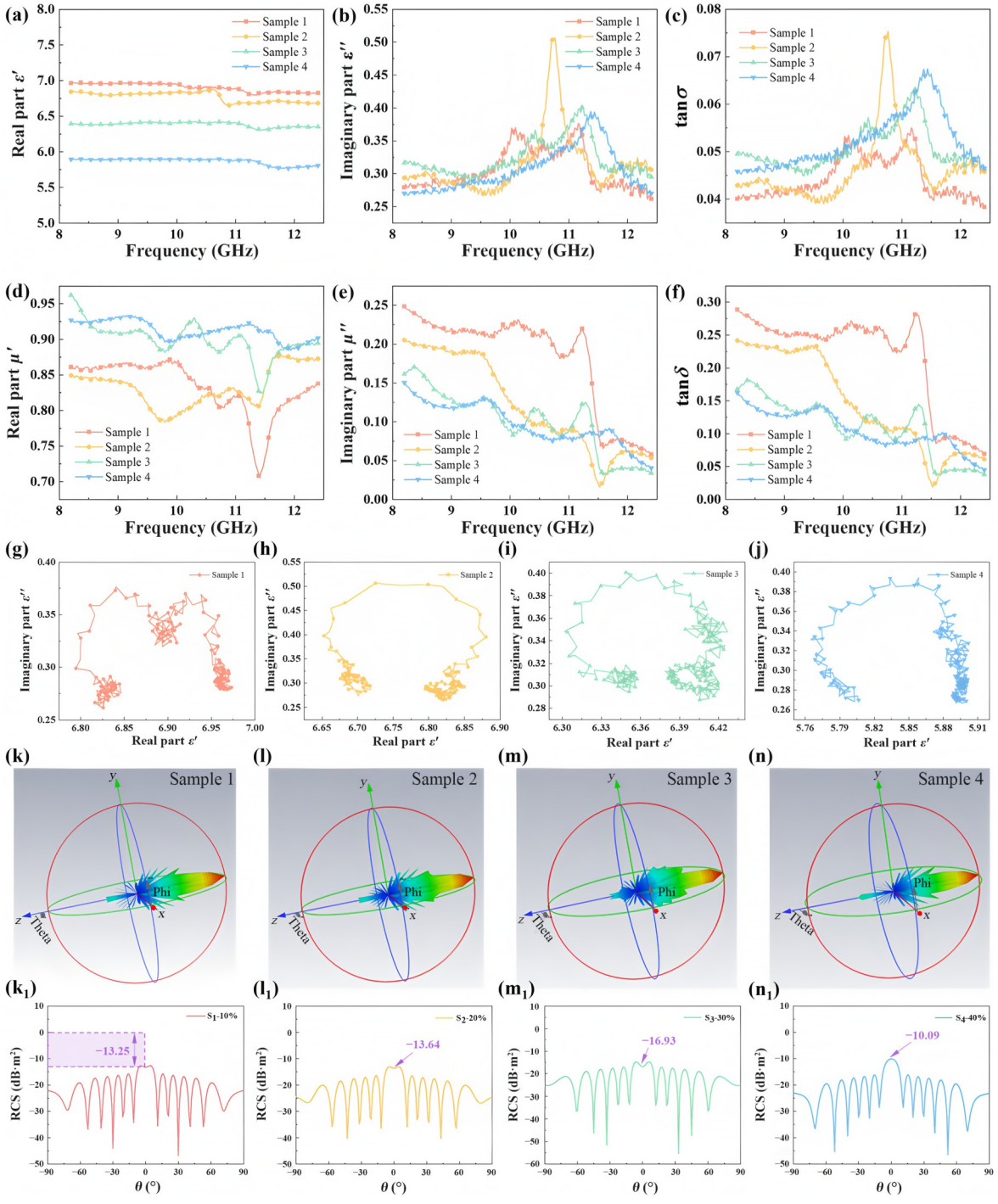

Figure 3 Electromagnetic parameters and RCS simulation results of the $Ni_3Sn_2S_2$@FeCoCrNiAl composite. (a)–(c) Dielectric constant of $Ni_3Sn_2S_2$@FeCoCrNiAl. (d)–(f) Magnetic permeability of $Ni_3Sn_2S_2$@FeCoCrNiAl. (g)–(j) Cole–Cole diagram of $Ni_3Sn_2S_2$@FeCoCrNiAl. (k)–(n) 3D radar scattering signals of $Ni_3Sn_2S_2$@FeCoCrNiAl; (k_1)–(n_1) RCS simulation curves of $Ni_3Sn_2S_2$@FeCoCrNiAl in the scattering angle range of −90° to 90°.

absorber, randomly oriented dipoles rearrange themselves under the influence of the electromagnetic field. In S1, the ε' value is relatively high at 6.69 and remains stable within the frequency band due to enhanced internal polarization caused by multi-phase coupling between metal elements in the high-entropy alloy matrix [54]. As the $Ni_3Sn_2S_2$ content increases, a continuous and dense coating gradually forms on the surface of the high-entropy alloy. Although the number of interfaces increases, the charge accumulation effect tends toward saturation, and the dielectric energy storage capacity stabilizes and slightly decreases. The ε' value of S3 is 6.42, and the ε' value of S4 decreases to 5.88. In Fig. 3(b), ε'' exhibits two local peaks (0.36–0.37) at 10.01 and 11.17 GHz, indicating the presence of local dipole responses and interface polarization in this frequency band. In S2, as $Ni_3Sn_2S_2$ gradually covers the surface completely, the interface polarization and conductive network enhance ε'', reaching 0.50 at 10.76 GHz. This demonstrates a significantly enhanced electromagnetic wave dissipation capability.

The 2D Kagome structure of $Ni_3Sn_2S_2$ provides stable conductive pathways, and its excellent electronic mobility enhances conductive loss, compensating for the insufficient dielectric polarization capability of FeCoCrNiAl itself. Correspondingly, in Fig. 3(c), the tanσ value reaches its maximum in S3, indicating that dielectric loss dominates the composite system at this point. In S4, despite the further increase in $Ni_3Sn_2S_2$ content, which restricts surface charge relaxation, the ε'' value decreases, weakening the energy conversion capability. As the $Ni_3Sn_2S_2$ content increases, the ε'' curve of S3 shows an overall improvement in the 8.2–12.4 GHz frequency band [55], indicating that the dielectric loss capability of $Ni_3Sn_2S_2$@FeCoCrNiAl is significantly enhanced. At lower $Ni_3Sn_2S_2$ contents, $Ni_3Sn_2S_2$@FeCoCrNiAl primarily relies on the magnetic loss contribution from the high-entropy alloy matrix, with relatively insufficient dielectric loss (Fig. 3(c)), resulting in lower tanσ values. As $Ni_3Sn_2S_2$ gradually increases and becomes uniformly distributed, polarization synergy within the material enhances, and the dominant role of dielectric loss gradually strengthens. The heterointerface between $Ni_3Sn_2S_2$ and the high-entropy alloy induces a large amount of interface polarization and dipole orientation, which helps improve the efficiency of electromagnetic wave energy dissipation.

The Ni-Kagome 2D metallic lattice structure in $Ni_3Sn_2S_2$ enhances electron mobility, endowing the composite material with robust conductive loss pathways and compensating for the relatively weak electrostatic polarization capability of the high-entropy alloy. In S3, the dense and uniform $Ni_3Sn_2S_2$ coating enables the construction of a multi-scale loss network, reinforcing the synergistic mechanism between electron transport and interfacial polarization. In contrast, although further increasing the $Ni_3Sn_2S_2$ content can continue to enhance conductivity, the introduction of excessive $Ni_3Sn_2S_2$ in S4 can easily cause impedance mismatch or even shielding effects, leading to impedance imbalance and preventing energy from being effectively absorbed into the material. Moreover, distinct from common semiconducting sulfides constrained by intrinsic bandgaps, the $Ni_3Sn_2S_2$ phase possesses a unique Ni-based Kagome lattice with metallic characteristics. This electronic structure ensures a high carrier density near the Fermi level, significantly facilitating electron migration and hopping under the alternating electromagnetic field. Consequently, the material exhibits stronger conductive loss capabilities compared to conventional semiconductors. Furthermore, the Kagome lattice ensures interfacial polarization and relaxation behaviors, further enhancing the dielectric dissipation capacity.

In Fig. 3(d), μ' represents the material's response to an alternating magnetic field, while μ'' (Fig. 3(e)) and tanδ reveal the magnetic loss mechanism [56]. For S1, μ' reaches 0.871 at 9.8 GHz and then gradually decreases to 0.70 at 11.39 GHz, indicating an initial increase in magnetic permeability followed by a rapid decline. Moreover, the tanδ of S1 shows a significant fluctuation at 11.5 GHz, indicating an enhanced effect of magnetic hysteresis and eddy current loss at this frequency, corresponding to a strong loss peak in the reflection coefficient. S3 exhibits a μ' of 0.96 at 8.2 GHz, which gradually decreases to 0.825 after 11.43 GHz, maintaining good magnetic response stability; its tanδ curve also shows a broader effective magnetic loss frequency band, reflecting a stronger synergistic dissipation mechanism between magnetic hysteresis and eddy currents[57, 58]. In contrast, the μ' of S4 reaches 0.930 at 9.2 GHz and then stabilizes, with a narrower magnetic response amplitude and reduced tanδ fluctuations (Fig. 3(f)). Its magnetic loss capability distribution is relatively balanced but less intense than that of S3. FeCoCrNiAl inherently contains strong magnetic elements such as Fe and Co, which provide fundamental magnetic loss pathways through natural resonance, exchange resonance, and magnetic coupling between components. The introduction of $Ni_3Sn_2S_2$ as a non-magnetic conductive phase does not significantly weaken the magnetic response. Instead, it introduces a large number of heterogeneous interfaces and microstructural discontinuities, which are beneficial for enhancing magnetic polarization and eddy current loss behavior in microwaves. The $Ni_3Sn_2S_2$ content in S3 reached the ideal coverage ratio, forming a complete electromagnetic synergy network, which provided the basis for its excellent microwave absorption performance.

The Cole–Cole plot reveals the polarization relaxation characteristics of the material by depicting the relationship between ε'' and ε' (Figs. 3(g)–3(j)). Ideally, regular arcs should be observed, indicating the superposition and coordination of multiple dielectric relaxation processes. The Cole–Cole curve for S1 in Fig. 3(g) consists of two discontinuous arc segments, indicating a dispersed distribution of polarization centers. S2 exhibits a smoother arc shape but oscillates within the low ε' range, revealing a discontinuous polarization process (Fig. 3(h)). S3 forms a more complete and clearly defined semi-arc shape spanning a broader ε' and ε'' range, indicating the presence of multiple mutually coupled polarization relaxation processes within it, including interface polarization, dipole orientation, and conductive relaxation, with the most potent synergistic effect (Fig. 3(i)). This well-developed polarization network corresponds to its excellent reflection loss performance. S4 also exhibits a semi-arc shape (Fig. 3(j)), but its radius and divergence are smaller than those of S3, indicating that its polarization intensity and synergistic effect are slightly weaker than those of S3. Thus, S3 demonstrates stronger microwave absorption capability compared to the other samples.

RCS is used to measure the scattering intensity of materials against incident radar waves and is an essential indicator for evaluating their electromagnetic stealth performance [59–61]. Figure 3 shows the three-dimensional (3D) directional diagram of RCS (Figs. 3(k)–3(n)) and the main reflection direction RCS values of $Ni_3Sn_2S_2$@FeCoCrNiAl composite materials with different $Ni_3Sn_2S_2$ contents. As the $Ni_3Sn_2S_2$ content increases from 10% to 30%, the main lobe reflection intensity gradually weakens, the side lobes increase, and the energy distribution becomes more uniform,

indicating that the material's surface scattering interference capability against incident waves has improved. The RCS value decreases from −13.25 to −16.93 dB (Figs. 3(k_1)–3(n_1)), achieving optimal stealth performance. This phenomenon is attributed to the formation of a dense, continuous conductive coating on the surface by an appropriate amount of $Ni_3Sn_2S_2$, which, together with the FeCoCrNiAl interface, constructs a multi-level polarization structure, significantly enhancing the dissipation and decoupling capabilities of electromagnetic waves and suppressing reflected echoes. In contrast, although the 40% sample contains more conductive phases, the main reflection lobe is re-enhanced, and the RCS value increases to −10.09 dB (Fig. 3(n_1)), indicating that excessive conductive phases cause impedance mismatch, thereby reducing stealth performance. Therefore, a 30% $Ni_3Sn_2S_2$ loading effectively optimizes microwave scattering paths and energy distribution, achieving excellent electromagnetic stealth capability.

To elucidate the relationship between the orbital contributions and atomic-scale effects of $Ni_3Sn_2S_2$@FeCoCrNiAl and its microwave absorption mechanism, DFT calculations were performed [62]. Figure 4 comprehensively analyzes, DOS, and differential charge density of the composite material (Fig. 4(a)). The DOS near the Fermi level is primarily contributed by the Fe/Co/Ni 3d orbitals from the alloy side (Figs. 4(b)–4(i)). It shows distinct resonance and orbital overlap between Fe/Co/Ni-3d states and the sulfide-side Ni-3d/S-3p states in the −3 to +2 eV range, indicating surface d-p hybridization and interfacial charge transfer [63]. The spin-up/spin-down DOS difference is minimal, exhibiting low spin polarization consistent with paramagnetic characteristics. As shown in Fig. 4(g), the differential charge density map reveals paired charge double layers at the heterointerface (blue/yellow representing electron gain/loss), with electron accumulation being more pronounced at the heterojunction [64]. The $\Delta\rho$ slice (Fig. 4(k)) shows pronounced charge rearrangement at the heterointerface, charge depletion on the FeCoCrNiAl side and accumulation on the $Ni_3Sn_2S_2$ side, indicating electron transfer from FeCoCrNiAl to $Ni_3Sn_2S_2$. The atomic neighbors exhibit a d–p lobe-like distribution, indicating metal–sulfur bonding hybridization. This charge transfer builds an interfacial dipole layer at equilibrium; under microwave excitation, this dipole layer undergoes lagged reorientation and rearrangement, producing interfacial polarization loss. This mechanism makes a

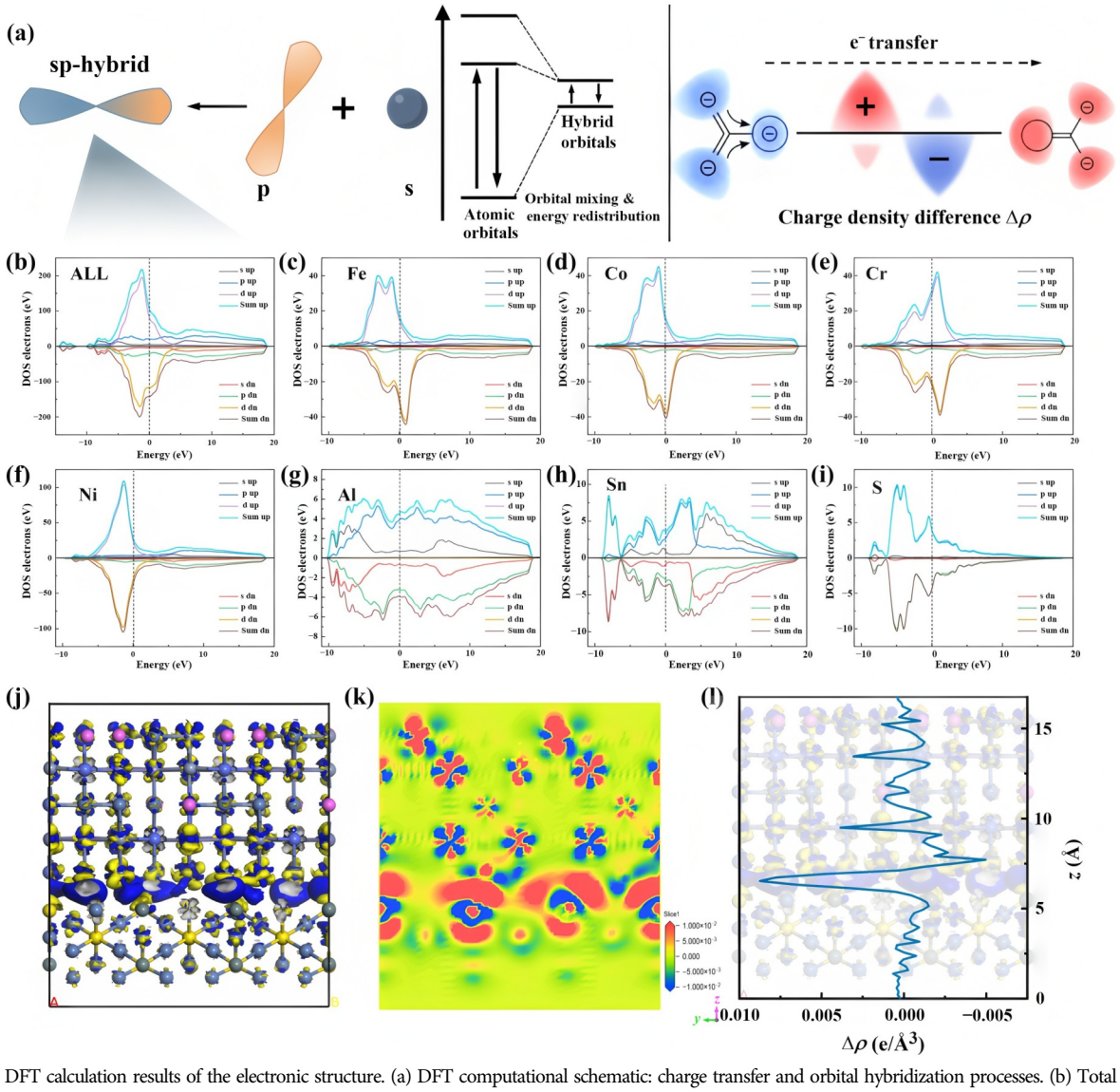

Figure 4 DFT calculation results of the electronic structure. (a) DFT computational schematic: charge transfer and orbital hybridization processes. (b) Total density of states. (c)–(i) Partial density of states. (j) Interfacial charge-density difference; (k) charge density difference $\Delta\rho$ slice; and (l) planar averaged charge density difference $\Delta\rho(z)$.

key contribution to the microwave absorption of the $Ni_3Sn_2S_2$@FeCoCrNiAl composite and provides electron-scale evidence for the enhancement of dielectric loss and impedance matching.

Figure 4(l) calculates the plane-averaged differential charge density $\Delta\rho(z)$ (e/Å^3) along the normal direction. $\Delta\rho(z)$ crosses zero at z_0 = 7.15 Å, with positive/negative peaks at 6.53 and 7.71 Å, exhibiting amplitudes of 8.75 × 10^{-3} and −4.96 × 10^{-3} e/Å^3, respectively, with an interpeak distance of approximately 1.19 Å and full width at half maximum of 0.99 and 0.59 Å, respectively. This indicates that the dipole layer is extremely thin, once again demonstrating that electrons transfer from FeCoCrNiAl to $Ni_3Sn_2S_2$, consistent with short-range interfacial screening and metallic system characteristics. At the same time, many "yellow/blue" small lobes are also observed between atomic pairs. This arises from the multicomponent electronegativity differences and coordination disorder within FeCoCrNiAl, and from electron shifts of countless micro-dipole polar bonds. These micro-dipoles relax under microwave irradiation, enhancing conductive losses and interfacial polarization losses, thereby providing the composite material with a broadband, highly efficient electromagnetic energy dissipation pathway. The above DFT-calculated structures confirm the proposed microwave absorption mechanism at the electronic-structure level.

Based on the above complex dielectric constant (ε_r) and complex magnetic permeability constant (μ_r), and based on transmission line theory, the electromagnetic wave reflection loss characteristics of the sample can be calculated using Eqs. (5) and (6)

$$Z_{in} = \sqrt{\frac{\mu_r}{\varepsilon_r}} \tanh\left[j\left(\frac{2\pi}{c}\right) fd\sqrt{\mu_r\varepsilon_r}\right] \quad (5)$$

$$\mathrm{RL\ (dB)} = 20\lg\left|\frac{Z_{in}-Z_0}{Z_{in}+Z_0}\right| \quad (6)$$

In the equations, Z_{in} is the input characteristic impedance of the material, Z_0 is the free space impedance, f is the electromagnetic wave frequency, d is the sample thickness, c is the speed of light, ε_r and μ_r are the complex dielectric constant and magnetic permeability of the sample, respectively.

Figure 5 shows the 3D RL spectrum plots of four sample groups at different thicknesses. At a thickness of 9.0 mm, although S1 in Fig. 5(a) reaches −25.63 dB at 11.8 GHz and exhibits a sharp absorption peak of −59.04 dB at 11.51 GHz, its absorption bandwidth is exceptionally narrow, failing to meet the practical requirements for wideband absorption. In Fig. 5(b), S2 shows a further deposition of $Ni_3Sn_2S_2$, resulting in an absorption valley of −38.32 dB at 11.05 GHz, with a significantly widened absorption bandwidth. The S3 exhibits the optimal absorption performance (Fig. 5(c)), with the RL_{min} value of −44.26 dB at 10.61 GHz. Additionally, its adequate absorption bandwidth (RL < −10 dB) is significantly expanded, covering the broadest range in the X-band (8.2–12.4 GHz), demonstrating dual advantages in both depth and bandwidth. Additionally, the $Ni_3Sn_2S_2$ coating in S3 exhibits a microstructure characterized by complete coverage and high-density crystallization, effectively extending the propagation path of electromagnetic waves within the material and inducing multiple scattering and loss processes, thereby enhancing electromagnetic energy dissipation efficiency. In contrast, in Fig. 5(d), although S4

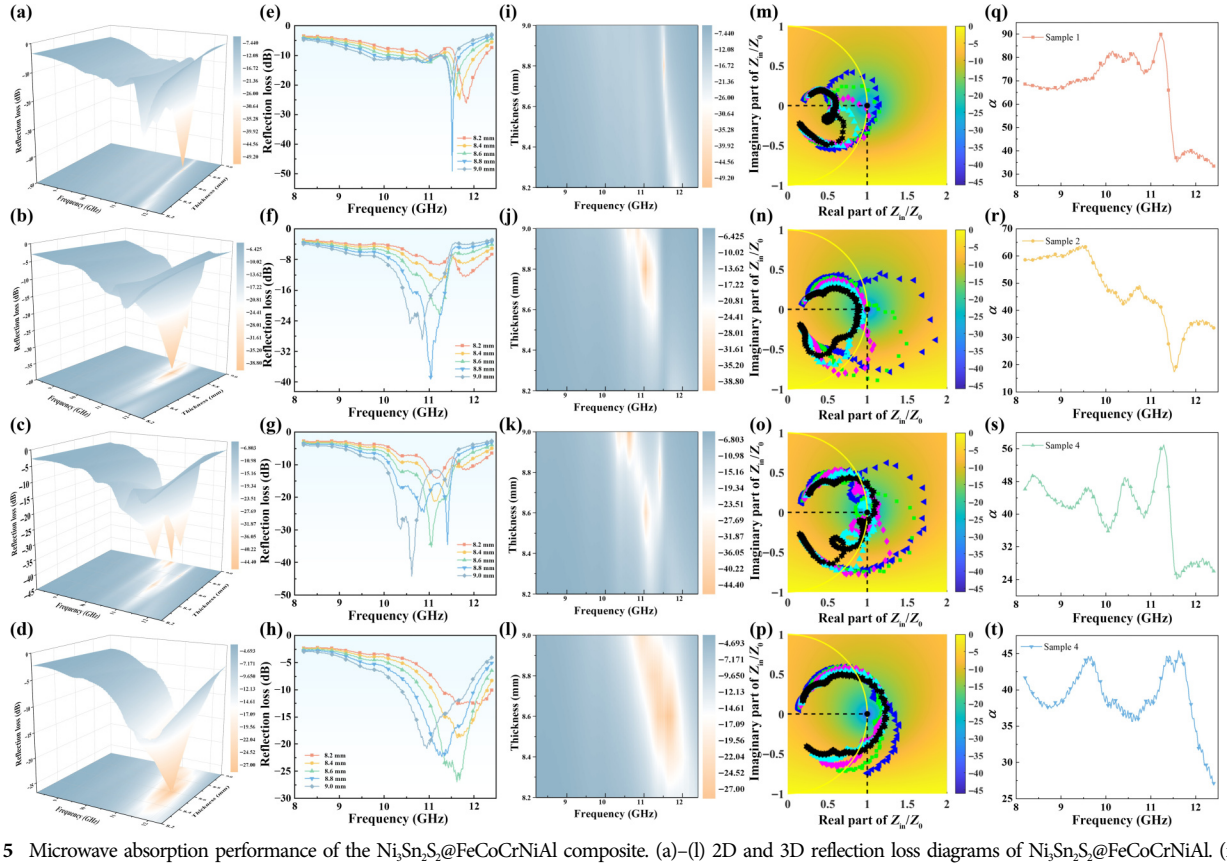

Figure 5 Microwave absorption performance of the $Ni_3Sn_2S_2$@FeCoCrNiAl composite. (a)–(l) 2D and 3D reflection loss diagrams of $Ni_3Sn_2S_2$@FeCoCrNiAl. (m)–(p) Smith charts of $Ni_3Sn_2S_2$@FeCoCrNiAl. (q)–(t) Attenuation coefficient plots of $Ni_3Sn_2S_2$@FeCoCrNiAl.

has the highest $Ni_3Sn_2S_2$ content, its RL peak reaches −26.9 dB at 11.62 GHz, resulting in degraded performance. This is due to the excessive thickness of the $Ni_3Sn_2S_2$ layer on the surface, causing impedance mismatch, while the thick coating also shields the underlying magnetic response, weakening magnetic loss.

Figures 5(m)–5(p) show the Smith charts clearly illustrating the frequency-dependent trajectories of the normalized input impedance (Z_{in}/Z_0) of the four sample groups in the complex plane. High-performance microwave absorption materials require the trajectories to converge as closely as possible to the center of the circle to achieve optimal energy incidence and minimal reflection. The Smith curves of the four groups of samples in the figure all converge spirally from high frequency to low frequency. The Smith curve of S1 deviates relatively from the center, briefly approaching the center in a "3" shape (Fig. 5(m)), but the overall trajectory is dispersed, indicating unstable impedance matching. S2 and S4 (Figs. 5(n) and 5(p)) approach the impedance matching circle in certain frequency bands, but only meet the matching conditions within narrow frequency bands. In contrast, S3 closely surrounds the central region compared to other samples (Fig. 5(o)), with the most concentrated trajectory passing through the matching circle, indicating optimal impedance matching for electromagnetic waves. Its reflection coefficient reaches −44.26 dB at 10.61 GHz while maintaining good matching across a wide frequency band, thereby achieving stable and deep absorption performance. For S4, the reflection loss performance degrades compared to S3. This degradation is attributed to the "metal-like shielding effect" caused by the overly dense shell. The dense $Ni_3Sn_2S_2$ layer leads to a shallow skin depth and a substantial drop in input impedance. As shown in the Smith chart (Fig. 5(p)), the impedance trajectory of S4 deviates significantly from the matching center. Consequently, the severe impedance mismatch causes incident electromagnetic waves to be reflected directly off the surface rather than penetrating into the absorber, demonstrating that optimizing impedance matching is critical for achieving superior microwave absorption.

The "self-sacrificing" synthesis strategy induces redistribution of surface elements in high-entropy alloys, thereby regulating impedance matching. During the reaction, Ni atoms are selectively consumed from the surface to form the dielectric $Ni_3Sn_2S_2$ shell, while the highly magnetic Fe and Co atoms are preserved within the alloy core. This naturally establishes a gradient heterostructure comprising a magnetic loss core and a dielectric loss shell. As shown in the Smith chart in Fig. 5(o), the optimized sample S3 exhibits a trajectory that spirals closely around the matching center point, confirming that the *in-situ* formed shell effectively regulates the input impedance and optimizes the impedance matching.

The attenuation coefficient α quantifies the rate of attenuation of electromagnetic waves in a material. The higher the value, the higher the absorption efficiency. In Fig. 5(q), the α of S1 increases from 68 Np/m at 8.2 GHz to 89.9 Np/m at 11.22 GHz, then rapidly decreases to 37 Np/m, before rising again to 39 Np/m and stabilizing, indicating strong absorption in the mid-to-high frequency range but with a narrow bandwidth. In Fig. 5(r), S2 has an α of approximately 63 Np/m at 9.5 GHz, but rapidly decreases to 17.9 Np/m at 11.5 GHz. S4 has an α peak of roughly 54 Np/m, with a stable curve, but its overall attenuation capability is moderate. In contrast, S3's attenuation coefficient remains stable at 52 Np/m across the entire X-band (Fig. 5(s)), gradually increasing to 54 Np/m at 11.5 GHz before slowly decreasing to 24 Np/m, demonstrating the widest bandwidth with sustained and balanced attenuation capability. This smooth and high-average-value α curve is consistent with S3's excellent impedance matching in the Smith chart and well-defined polarization relaxation in the Cole–Cole plot, confirming that the $Ni_3Sn_2S_2$@FeCoCrNiAl composite material effectively achieves synergistic effects among multiple electromagnetic loss mechanisms, significantly enhancing the absorption and dissipation capabilities of electromagnetic waves.

To further enhance the absorption performance of the $Ni_3Sn_2S_2$@FeCoCrNiAl composite absorber material in the low-frequency range and optimize its thickness, as shown in Fig. 6(a), this study introduces a frequency-selective surface (FSS) with a periodic structure. The FSS serves as a structural functional layer that can generate strong resonant responses at specific frequencies. Combined with the dielectric loss, magnetic loss, and interface polarization mechanisms within the material, this significantly enhances the microwave absorption performance of the $Ni_3Sn_2S_2$@FeCoCrNiAl composite material. Figure 6(b) shows four different shapes of FSS graphic units, all arranged with a period of c = 10 mm and a thickness controlled between 1.0 and 2.0 mm. Each structure achieves electromagnetic wave control by combining different central and corner graphics. The unit structure in Fig. 6(c) combines a central cross-shaped pattern with square corner patterns of d_1 = 2 mm. When the thickness is 1.8 mm, the reflection loss reaches −60.47 dB at 10.06 GHz, with an adequate absorptive bandwidth spanning 8.59–10.3 GHz, while significantly optimizing the thickness of the silicone rubber. Further inspection of the EM-field and surface-current distributions (Fig. 6) shows that, in P_1, the *E*-field forms paired hotspots along the top and bottom edges， a typical gap-capacitance effect that drives interfacial charge accumulation and dipole relaxation, the *H*-field concentrates at the unit center, consistent with a magnetic dipole from closed current loops, and the surface current density exhibits both a central peak and edge eddy currents, reflecting the synergistic effects of Ohmic and eddy current losses. This structure enables localized surface current concentration, inducing dipole resonance and electric field enhancement effects, while the central cross structure generates stable electric dipole responses. Figure 6(d) retains the central cross structure while modifying the corner patterns to rectangles with c = 10 mm and d_4 = 1 mm. At 9.90 GHz, a loss peak of −32.04 dB is observed with a silicone rubber thickness of 2.0 mm, P_2 exhibits a broader *E*-field hotspot zone with a more compact central *H*-field, accompanied by a synchronous increase in equivalent capacitance and inductance, the surface current density becomes more continuous with more ordered vortices. Indicating that edge geometric adjustments can significantly influence resonance coupling efficiency.

Furthermore, while maintaining the edge shape of the FSS unchanged, Fig. 6(e) optimizes the central pattern into a hollow hexagon with an outer diameter of d_5 = 3 mm and an inner diameter of d_6 = 1 mm to systematically investigate its regulatory mechanism on impedance matching. It can be observed that at a thickness of 2 mm, a reflection loss peak of −36.22 dB appears at 9.72 GHz. This centrally symmetric unit structure enables electromagnetic waves to form multiple resonant cavities on the structural surface, achieving repeated scattering and dissipation of energy. The E-field transitions into top–bottom banded patterns with inter-unit coupling, activating a larger volume of interfacial dipoles, the *H*-field's central band broadens, with the fundamental and higher-order modes coexisting, the surface current density forms a mesh-like multi-vortex network that lengthens current

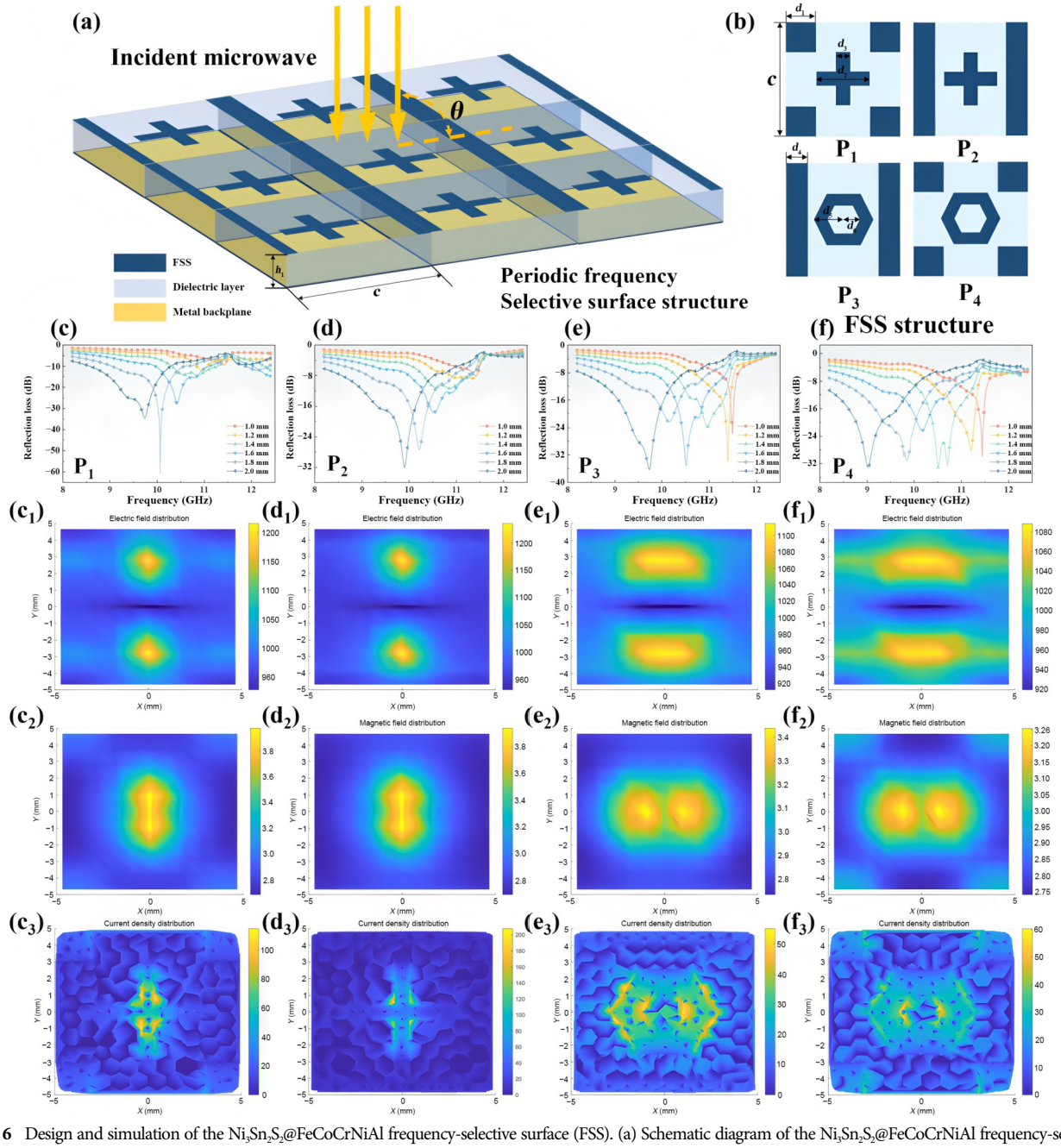

Figure 6 Design and simulation of the $Ni_3Sn_2S_2$@FeCoCrNiAl frequency-selective surface (FSS). (a) Schematic diagram of the $Ni_3Sn_2S_2$@FeCoCrNiAl frequency-selective structure. (b) Schematic diagram of the FSS pattern P_1–P_4. (c)–(f) Reflection loss after adding the frequency-selective structure. (c_1)–(f_1) Electric field distribution. (c_2)–(f_2) Magnetic field distribution. (c_3)–(f_3) Current density distribution.

paths and strengthens both ohmic and eddy-current losses, thereby widening the bandwidth. Figure 6(f) adopts the same hollow hexagonal central structure while restoring the corner designs of the four squares corners from Fig. 6(b) (P_1). At a thickness of 2.0 mm, it demonstrates broadband absorption capability, with an effective absorption bandwidth covering 8.2–10.0 GHz, spanning half of the entire X-band. The optimal absorption bandwidth further shifts toward lower frequencies. In Figs. 6(f_1)–6(f_3), the continuous strip-like *E*-field establishes inter unit surface-wave channels, the *H*-field shows superposed circulating loops, yielding a response more robust to incidence angle and polarization, and the surface current density exhibits annular and multi-core vortices with enlarged loop areas and tortuous paths. Under the joint action of the $Ni_3Sn_2S_2$ Kagome network and the high-entropy alloy metallic substrate, these features further amplify the effective surface resistance and eddy-current dissipation. Through the synergistic design of multiple rectangles and hollow polygons, also exhibits good absorption performance at smaller thicknesses, such as 1.8 and 1.4 mm, fully demonstrating its significant advantages in enhancing low-frequency response and reducing matching thickness.

Figure 7(a) shows the effect of $Ni_3Sn_2S_2$ content on the thermal conductivity of $Ni_3Sn_2S_2$@FeCoCrNiAl silicone rubber composite materials. We prepared composite silicone rubber. samples with $Ni_3Sn_2S_2$ contents of 10%, 20%, 30%, and 40%, and monitored the heating process in real time using infrared thermal imaging technology at equidistant time intervals of 2, 5, and 8 s (Fig. 7(c)),

extracting and analyzing the central temperature change data for comparison [65, 66]. The results indicate that under the same heating time, the thermal conductivity of the composite material does not increase linearly with the increase in $Ni_3Sn_2S_2$ content. As shown in Fig. 7(a), the 30% $Ni_3Sn_2S_2$ sample exhibits the best thermal conductivity, with the largest increase in central temperature during the heating process, reaching a final temperature increase of 104.3 °C, significantly higher than other groups (10%, 20%, and 40% samples were 60.7, 68.0, and 84.3 °C, respectively). This performance improvement is attributed to the fact that at a 30% content, $Ni_3Sn_2S_2$ can better coat the FeCoCrNiAl surface, forming a continuous and uniform thermal conductivity network within the FeCoCrNiAl matrix, thereby enhancing the synergistic heat transfer effect of electrons and phonons. As a high-entropy alloy, FeCoCrNiAl exhibits excellent thermal conductivity, with its multi-component solid solution structure providing a high density of metallic bonds that facilitate efficient heat carrier transport. $Ni_3Sn_2S_2$ adopts a Shandite type structure, and the 2D Kagome network formed by Ni atoms further aids electronic heat conduction. At a 30% content, the synergistic effect between the two is optimized, with the filler uniformly dispersed in the silicone rubber matrix, resulting in low interfacial thermal resistance and continuous thermal conduction pathways. However, when the content is further increased to 40%, $Ni_3Sn_2S_2$ particles may agglomerate, leading to localized increases in thermal resistance and disrupting the continuity of the original thermal conduction network, thereby inhibiting effective heat conduction within the system. This phenomenon can be interpreted by the unique phonon transport behavior within the Kagome network. The specific triangular geometric structure of the Kagome lattice introduces inherent lattice anharmonicity, effectively shortening the phonon mean free path. Although the metallic shell facilitates electron thermal transport, in the thick shell of S4, this intrinsic phonon scattering effect becomes pronounced, impeding effective heat transfer and thereby limiting the further enhancement of the overall thermal performance. For comparison, the heating performance of the pure FeCoCrNiAl HEA was evaluated under identical conditions. Its surface temperatures reached only 31.1,

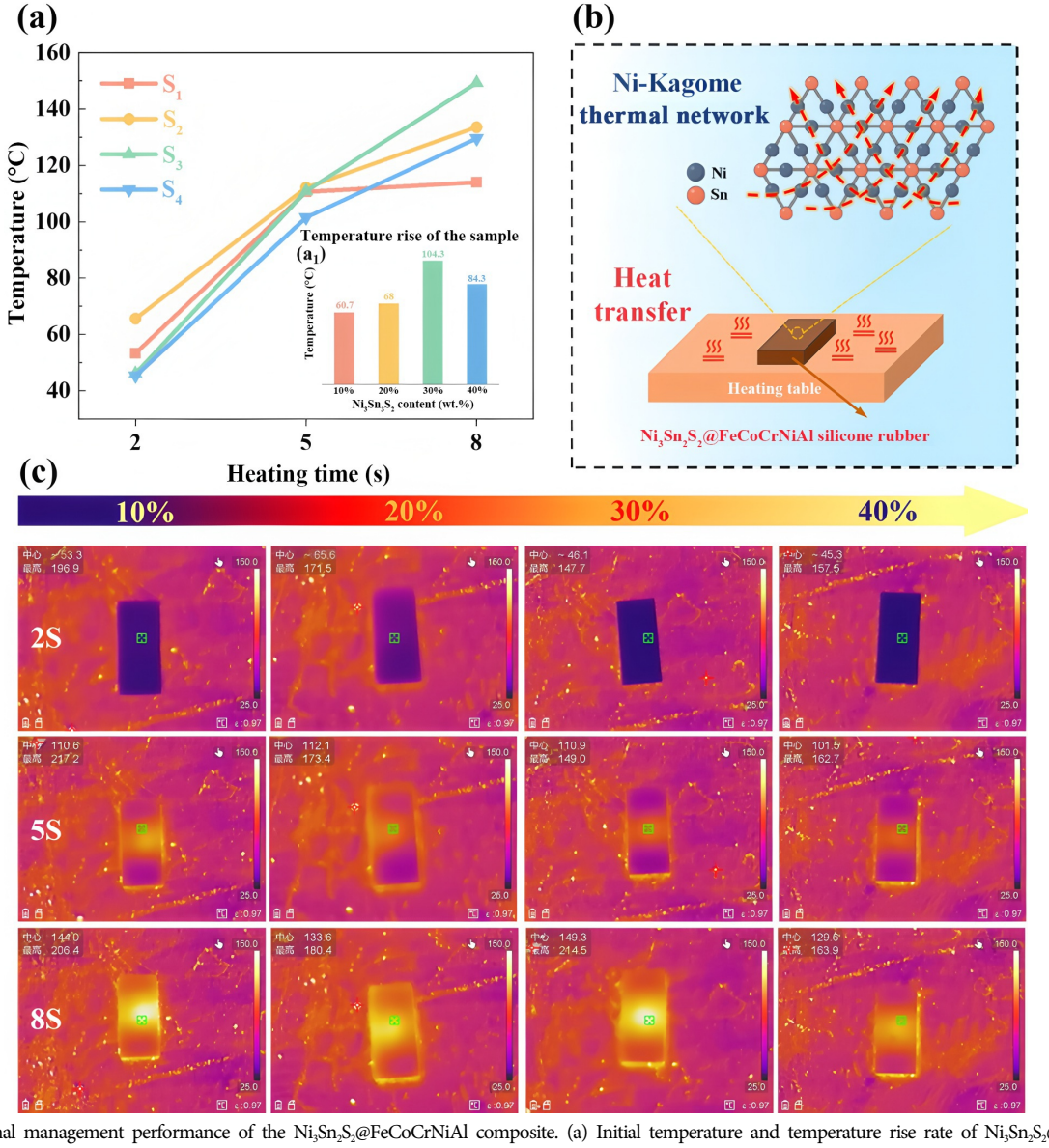

Figure 7 Thermal management performance of the $Ni_3Sn_2S_2$@FeCoCrNiAl composite. (a) Initial temperature and temperature rise rate of $Ni_3Sn_2S_2$@FeCoCrNiAl. (b) Thermal conductivity mechanism of $Ni_3Sn_2S_2$@FeCoCrNiAl composite powder. (c) Infrared thermal imaging of $Ni_3Sn_2S_2$@FeCoCrNiAl.

58.0, and 91.0 °C at 2, 5, and 8 s, respectively. This significant performance gap underscores the contribution of the $Ni_3Sn_2S_2$ shell. The inherent metallic nature and unique Kagome lattice of the sulfide coating facilitate efficient electron and phonon transport, thereby constructing a continuous thermal conduction network that effectively enhances the thermal conductivity of the heterostructure.

The excellent electromagnetic loss properties of the $Ni_3Sn_2S_2$@FeCoCrNiAl composite material are attributed to the synergistic effects of multiple mechanisms. The dielectric loss primarily stems from the excellent conductivity of $Ni_3Sn_2S_2$ and the electric dipole response and interface polarization induced by its Kagome metallic lattice structure. The absorption mechanism is illustrated in Fig. 8. At the nanoscale, numerous heterogeneous interfaces form between $Ni_3Sn_2S_2$ and the high-entropy alloy matrix, effectively enhancing spatial charge accumulation and polarization relaxation. Magnetic loss is provided by FeCoCrNiAl. The interaction of multiple magnetic elements in the material results in the coexistence of natural resonance and exchange resonance, while changes in the magnetic domain structure within the particles cause hysteresis loss. As the content of $Ni_3Sn_2S_2$ increases, the interface density rises, enabling the construction of a multi-scale synergistic network that enhances both conductive loss and magnetic response capability. Additionally, the *in-situ* generation and diffusion behavior of Ni form dense, continuous conductive pathways, further enhancing energy dissipation and significantly improving the overall microwave absorption performance of the composite material.

4 Conclusion

This study proposes an innovative method using FeCoCrNiAl high-entropy alloy itself as a Ni source, successfully constructing a $Ni_3Sn_2S_2$ nanocoating with a Shandite structure on its surface using an *in-situ* hydrothermal method. The Ni-Kagome metallic lattice structure of $Ni_3Sn_2S_2$ forms a continuous conductive and thermal network on the surface of the FeCoCrNiAl high-entropy alloy, enhancing its microwave absorption and thermal conductivity properties. When the loading of $Ni_3Sn_2S_2$ reaches 30 wt.%, the performance is optimal. S3 exhibits a minimum reflection loss of −44.26 dB at 10.61 GHz. After introducing a FSS into S2, the absorption thickness is optimized to 1.4 mm, and the reflection loss is further reduced to −60.47 dB. In terms of thermal conductivity, S3 demonstrated the best thermal conductivity, with a temperature rise of 104.3 °C within 8 s. RCS simulation results indicate that the S3 sample achieves a scattering suppression of −16.93 dB at a frequency of 15 GHz. This study validates that the $Ni_3Sn_2S_2$ nanocoating, as a functional interface phase, can significantly synergistically enhance the electromagnetic absorption and thermal conductivity performance of high-entropy alloy-based composite materials, providing a new approach for developing multifunctional integrated microwave absorption materials with a multi-loss synergistic mechanism.

Data availability

All data needed to support the conclusions in the paper are presented in the manuscript and the Electronic Supplementary Material. Additional data related to this paper may be requested from the corresponding author upon request.

Acknowledgements

This study was funded and supported by the National Natural Science Foundation of China (No. 22378249), Aeronautical Science Foundation (No. 2024Z056111001), Shaanxi Province Innovation Capacity Support Program Project (No. 2025ZC-KJXX-104), Scientists and Engineers Team Construction Project of Qin Chuangyuan (No. 2024QCY-KXJ-122), and Scientific and Technological Program of Shaanxi Provincial Department of Education (No. 24JR068).

Declaration of competing interest

All the contributing authors reports no conflict of interests in this work.

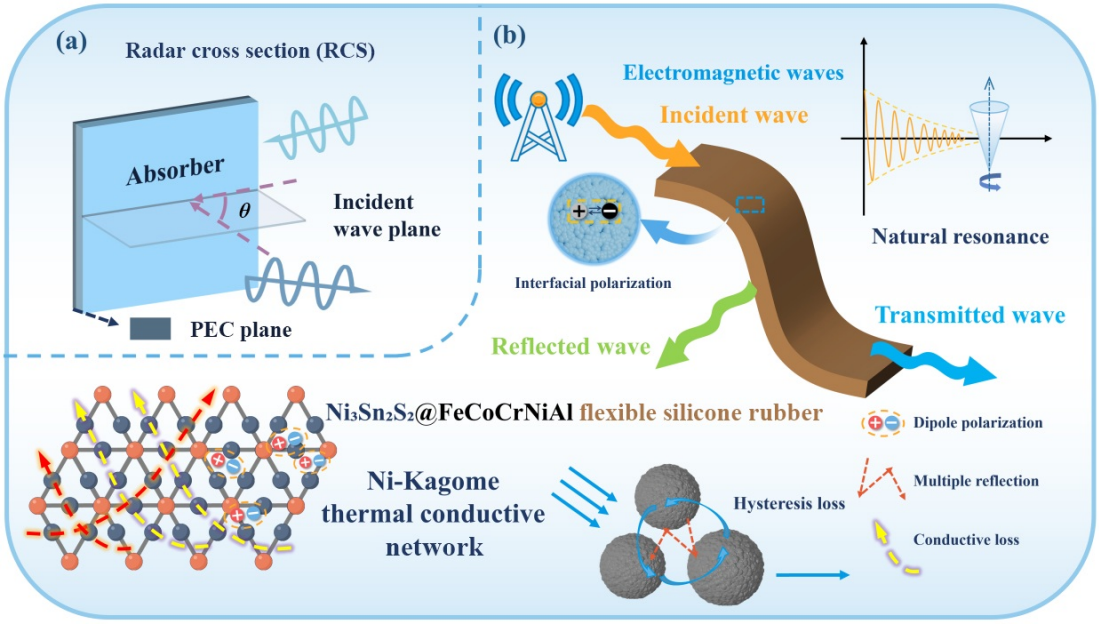

Figure 8 (a) RCS simulation schematic diagram. (b) $Ni_3Sn_2S_2$@FeCoCrNiAl wave absorption mechanism diagram.

Author contribution statement

H. P. X.: Conceptualization, investigation, visualization, writing – original draft. Y. L.: Methodology, formal analysis, writing – review & editing. X. H. Z.: Resources, supervision. Q. W.: Conceptualization, investigation. W. X. Z.: Resources, supervision. L. Z.: Validation, data curation. X. L. S.: Supervision, funding acquisition, project administration. C. Y. X.: Supervision, writing – review & editing. All the authors have approved the final manuscript.

Use of AI statement

None.

References

[1] Qi, J. M.; Liang, C. B.; Ruan, K. P.; Li, M. K.; Guo, H.; He, M. K.; Qiu, H.; Guo, Y. Q.; Gu, J. W. Cactus-like architecture for synergistic microwave absorption and thermal management. *Nat. Sci. Rev.* **2025**, *12*, nwaf394.

[2] Meng, Y. T.; Cai, B.; Zhou, Y. T.; Zhou, L.; Zhang, Y.; Wang, J. H.; Sarula, G.; Yan, L. T.; Lu, M.; Liang, B. L. et al. Bionic coral reef inspired enhanced scattering of trimetallic LDH self assembled $Ti_3C_2T_x$ MXene for advanced microwave absorption. *Nano Res.* **2025**, *18*, 94907842.

[3] Zhang, Y. L.; Ruan, K. P.; Zhou, K.; Gu, J. W. Controlled distributed $Ti_3C_2T_x$ hollow microspheres on thermally conductive polyimide composite films for excellent electromagnetic interference shielding. *Adv. Mater.* **2023**, *35*, 2211642.

[4] Dong, W. W.; Tu, S. H.; Rehman, S. U.; Chen, C. C.; Luo, X. G.; Liang, T. X.; Hu, Y. F.; Wang, L. Balancing electromagnetic wave loss capability and impedance matching of MOF derived porous carbon composite FeSiB based soft magnetic alloys to optimize the absorption performance. *Chem. Eng. J.* **2025**, *517*, 164370.

[5] He, H.; Wang, Z. X.; Xie, C. H.; Qian, Y. X.; Gang, S.; Tao, Y.; Long, H.; Zhang, W. G.; Luo, Y. B.; Jiang, Q. H. et al. Layered double hydroxide embedded in loofah-derived biocarbon composites towards broadband electromagnetic wave absorption and enhanced flame retardancy. *Carbon* **2025**, *243*, 120526.

[6] Peng, H. L.; Xiong, Z. Q.; Gan, Z. H.; Liu, C. H.; Xie, Y. Microcapsule MOFs@MOFs derived porous “nut-bread” composites with broadband microwave absorption. *Compos. Part B: Eng.* **2021**, *224*, 109170.

[7] Zhou, Y. X.; Zhang, Y. L.; Pang, Y. H.; Guo, H.; Guo, Y. Q.; Li, M. K.; Shi, X. T.; Gu, J. W. Thermally conductive $Ti_3C_2T_x$ fibers with superior electrical conductivity. *Nano-Micro Lett.* **2025**, *17*, 235.

[8] Yu, L. H.; Lian, G. J.; Zhu, G. Z.; Ren, S. E.; Du, Y. F.; Xiong, X. H.; Chen, R.; Zhang, J. C.; You, W. B.; Che, R. C. Hollow FeCoNiAl microspheres with stabilized magnetic properties for microwave absorption. *Nano Res.* **2024**, *17*, 2079–2087.

[9] Han, Y. X.; Yang, Y. R.; Li, T. H.; Zhang, Y. L.; Guo, H.; He, M. K.; Han, K. H.; Qiu, H.; Gu, J. W. Hierarchical heterogeneous Co-based magnetic absorbers for superior broadband high-efficiency microwave absorption. *Adv. Funct. Mater.*, **2016**, *36*, 25719.

[10] Wang, B. L.; Ni, C.; Ding, M. C.; Zhao, D. M.; Duan, Z. Y.; Xie, X. B.; Li, C. W. Hierarchically pepper wood-like Co_3Fe_7@C nanotubes for broadband microwave absorption and efficient electromagnetic interference shielding. *J. Mater. Sci. Technol.* **2026**, *244*, 196–207.

[11] Zhang, X.; Xiang, Z.; Yao, K.; Wang, X.; Jiang, H. J.; Wang, J. L.; Lu, W. Hydrangea-like N-doped Carbon/MoO_2@SnS_2 microspheres with Schottky contact: A multi-interface heterostructure for high-performance microwave absorption. *Compos. Part B: Eng.* **2023**, *263*, 110858.

[12] Ming, W.; Yang, L.; Chen, H. X.; Fei, F.; Zhang, H.; Sarula, G.; Wang, J. H.; Wang, T. Y.; Jin, C. Z.; Liang, B. L. et al. High toughness MXene/ANF-CZIF67/ANF "magnetic-electric" Janus film for multifunctional low reflection electromagnetic interference shielding. *Nano Res.* **2025**, *18*, 94907621.

[13] Zhang, Y. L.; Gu, J. W. Ultrathin and flexible electromagnetic interference shielding films by interface-confinement strategy. *Sci. China Mater.*, in press, DOI: 10.1007/s40843-025-3876-5.

[14] Wang, T. X.; Xiong, C. Y.; Zhang, Y. K.; Wang, B.; Xiong, Q.; Zhao, M. J.; Ni, Y. H. Multi-layer hierarchical cellulose nanofibers/carbon nanotubes/vinasse activated carbon composite materials for supercapacitors and electromagnetic interference shielding. *Nano Res.* **2024**, *17*, 904–912.

[15] Xie, X. B.; Liu, R. L.; Zhang, Y. H.; Ni, C.; Ma, Y. K.; Zhao, Y. F.; Du, W.; Wang, B. L. Fabrication of 3D $Fe_{0.64}Ni_{0.36}$-CNTs/carbon foam hybrid composites for strong wideband electromagnetic wave absorption at thin thickness. *J. Mater. Sci. Technol.* **2025**, *239*, 16–27.

[16] Wang, Q.; Liu, Y.; Su, E. D.; Su, X. L. Influence of reducing agent concentration on properties of flexible microwave absorbing coating containing silver coated FeSiAl powders. *Mater. Today Nano* **2025**, *29*, 100603.

[17] Zhao, J.; Lai, H. R.; Li, M. Anchoring 1T-MoS_2 petals on N-doped reduced graphene oxide for exceptional electromagnetic wave absorption. *Int. J. Miner. Metall. Mater.* **2025**, *32*, 619–630.

[18] Li, X. J.; Shen, M. X.; Sun, J. J.; Xiong, C. Y.; Liu, Y. J.; Hou, L.; Hua, F. G. Bottom-up assembly of biomass-derived MXene aerogels with hierarchical electromagnetic interfaces for multifunctional electromagnetic wave absorption. *Small* **2025**, *22*, e10286.

[19] Zhang, W. D.; Zhang, X.; Wu, H. J.; Yan, H. X.; Qi, S. H. Impact of morphology and dielectric property on the microwave absorbing performance of MoS_2-based materials. *J. Alloys Compd.* **2018**, *751*, 34–42.

[20] Wang, J. N.; Chen, Y. K.; Rao, H. C.; An, X. P.; Nan, K.; Wang, Y. Constructing Schottky contacts via vertical growth of SnS_2 nanosheets on hollow microspheres for efficient microwave absorption. *J. Mater. Sci. Technol.* **2025**, *232*, 147–155.

[21] Yang, Z. Y.; Feng, D.; Xie, Y. H.; Wu, F.; Mei, Y.; Zhang, T. Y.; Xie, D. L. Exploring the synergistic role of graphite and binary metal sulfides in achieving superior electromagnetic wave absorption. *Compos. Part A: Appl. Sci. Manuf.* **2025**, *191*, 108751.

[22] Wang, Q.; Su, X. L.; Jia, Y.; Liu, Y.; Shahzad, F. Microwave absorption properties and electromagnetic characteristics of MoS_2/MXene sandwich composites. *Ceram. Int.* **2025**, *51*, 9833–9841.

[23] Wang, L.; Yang, Z. L.; Lang, L.; Men, J. Y.; Gao, T. T.; Wang, Q.; Cheng, J. W.; Liu, Y. Z.; Zheng, N.; Liu, J. et al. Flexible multifunctional MXene/polyimide films with Janus structure for superior electromagnetic interference shielding. *Adv. Compos. Hybrid Mater.* **2025**, *8*, 26.

[24] Lin, H. D.; Zhang, X.; Zhang, B. L.; Huang, L. K.; Fang, J.; He, X. H.; Li, J. W. Triboelectric mechanism enhances piezoelectric performance of polyimide composite nanofibrous membrane. *Compos. Sci. Technol.* **2025**, *269*, 111231.

[25] He, M. K.; Zhong, X.; Lu, X. H.; Hu, J. W.; Ruan, K. P.; Guo, H.; Zhang, Y. L.; Guo, Y. Q.; Gu, J. W. Excellent low-frequency microwave absorption and high thermal conductivity in polydimethylsiloxane composites endowed by hydrangea-like CoNi@BN heterostructure fillers. *Adv. Mater.* **2024**, *36*, 2410186.

[26] Guo, Y. Q. Li, P.; Zhao, R. L.; Gu, J. W. Preparation and mechanism of thermally conductive polyimide phase change composites with electromagnetic wave-absorbing performance. *Acta Polym. Sin.* **2025**, *56*, 2347–2360.

[27] Zhang, L.; Li, Z. Q.; Shang, S. H.; Liu, Y.; Zhang, X. M.; Chen, H. T.; Ji, H. J.; Zheng, W. X.; Liu, K. P.; Zhu, Z. et al. Asymmetric wettability sandwich-structured MXene@CuS/CNF film for selective antibacterial/anti-adhesion surfaces and EMI shielding in wearable

electronics. *Chem. Eng. J.* **2026**, *527*, 172128.
[28] Wang, T. X.; Xiong, C. Y.; Li, P. Y. Manufacturing strategies for cellulose-based EMI shielding composites: Process-driven microstructures and EMI shielding performance. *Compos. Part B: Eng.* **2026**, *309*, 113093.
[29] Chen, H. Y.; Gao, L.; Dong, J, Qu, Y. P.; Gao, H. Research on regulation and wave-absorption properties of porous $Na_3Zr_2Si_2PO_{12}$ ceramics. *Basic Sci. J. Text. Univ.* **2025**, *38*, 50–57.
[30] Ma, Y. M.; Liu, Y.; Su, E. D.; Wang, Q.; Luo, F.; Su, X. L. Preparation and electromagnetic absorption properties of silver-decorated polystyrene with frequency-selective surfaces. *J. Mater. Sci.* **2024**, *59*, 12984–12997.
[31] Cai, Y. Z.; Chai, Y. L.; Cheng, L. F.; Guo, S. Y.; Yuan, Y. B.; Huang, X.; Yu, Z. X.; Chen, M. X.; Ren, S. X.; Yuan, H. D. N-doped CNTs/CoNi nanochains-carbon hollow microspheres multi-level multi-scale heterogeneous interface structures and microwave absorption properties. *Carbon* **2024**, *228*, 119423.
[32] Wang, L.; Lang, L.; Hu, X.; Gao, T.; He, M.; Qiu, H.; Ji, X.; Guo, H.; Zhang, Y.; Huang, S. Multifunctional ionic bonding-strengthened ($Ti_3C_2T_x$ MXene/CNF)-(BNNS/CNF) composite films with Janus structure for outstanding electromagnetic interference shielding and thermal management. *J. Mater. Sci. Technol.* **2025**, *224*, 46–55.
[33] Xie, L.; Liu, R. L.; Jiang, X. M.; Ni, C.; Wang, B. L.; Hou, C. X.; Lan, D.; Du, W.; Xie, X. B. Carbon induced multiple interfaces and *in-situ* formed defects in oxidation of Co toward enhancing microwave absorption performances. *Carbon* **2025**, *238*, 120272.
[34] Wang, Q.; Liu, Y.; Ma, Y. M.; Su, E. D.; Su, X. L. Preparation and electromagnetic property of Ag@FeSiAl/polyurethane resin flexible absorption wave coating. *J. Alloys Compd.* **2025**, *1021*, 179666.
[35] Jiang, Z. Y.; Gao, Y. J.; Pan, Z. H.; Zhang, M. M.; Guo, J. H.; Zhang, J. W.; Gong, C. H. Pomegranate-like ATO/SiO_2 microspheres for efficient microwave absorption in wide temperature spectrum. *J. Mater. Sci. Technol.* **2024**, *174*, 195–203.
[36] Zhao, W. B.; Ding, Y.; Lu, C. H. Influence of wet milling duration on the electromagnetic properties and microwave absorption performances of $FeCoNiAl_{0.2}Si_{0.3}$ high-entropy alloy. *Powder Technol.* **2025**, *452*, 120522.
[37] Duan, Y. P.; Li, Z. R.; Liu, X. J.; Pang, H. F.; Huang, L. X.; Sun, X. Y.; Shi, Y. P. Optimized microwave absorption properties of $FeCoCrAlGd_x$ high-entropy alloys by inhibiting nanograin coarsening. *J. Alloys Compd.* **2022**, *921*, 166088.
[38] Wang, H. H.; Xiao, X. Y.; Zhai, S. R.; Xue, C.; Zheng, G. P.; Zhang, D. Q.; Che, R. C.; Cheng, J. Y. Spontaneous orientation polarization of anisotropic equivalent dipoles harnessed by entropy engineering for ultra-thin electromagnetic wave absorber. *Nano-Micro Lett.* **2025**, *17*, 19.
[39] Zhang, Y. Y.; Li, Z. R.; Chen, K. W.; Li, L.; Uher, C. Extremely large magnetoresistance and quantum oscillations in semimetal $Ni_3In_2S_2$. *Mater. Today Phys.* **2024**, *40*, 101318.
[40] Lv, S. H.; Guo, H.; Qi, Q.; Li, Y. H.; Hu, G. J.; Zheng, Q.; Wang, R. W.; Si, N.; Zhu, K.; Zhao, Z. et al. Field-induced butterfly-like anisotropic magnetoresistance in a kagome semimetal $Co_3In_2S_2$. *Adv. Funct. Mater.* **2025**, *35*, 2412876.
[41] Kolivand, N.; Haghighat-Shishavan, S.; Nazarian-Samani, M.; Kheradmandfard, M.; Nazarian-Samani, M.; Kashani-Bozorg, S. F.; Lee, W. Firmly interlocked Janus-type metallic $Ni_3Sn_2S_2$-carbon nanotube heterostructure suppresses polysulfide dissolution and Sn aggregation. *J. Colloid Interface Sci.* **2023**, *648*, 406–417.
[42] Ma, L.; Hu, R.; Kang, C. X.; Fu, L. K.; Chen, Y. C.; Liu, H. J.; Liu, Q. M. Facile synthesis of three-dimensional $Ni_3Sn_2S_2$ as a novel battery-type electrode material for high-performance supercapacitors. *Electrochim. Acta* **2021**, *396*, 139216.
[43] Krishnaiah, M.; Kumar, A.; Song, J.; Jin, S. H. Cu/(Co+Sn) ratio effects on physical and photodetective properties for visible light absorbing Cu_2CoSnS_4 nanoparticles via a one-pot hydrothermal process. *J. Alloys Compd.* **2020**, *847*, 156174.
[44] Jin, Y. H.; Han, J. H.; Park, J.; Kim, M.; Seok, S. H.; Chae, Y.; Sim, Y.; Seo, S.; Lee, H.; Wang, J. et al. Water- and oxidation-resistant MXenes for advanced electromagnetic interference shielding applications. *InfoMat* **2025**, *7*, e70034.
[45] Hu, F. Y.; Zhang, P. G.; Wu, F. S.; Tian, Z. H.; Tang, H. F.; Fan, B. B.; Zhang, R.; Sun, W. W.; Cai, L. Z.; Sun, Z. M. One-dimensional core-sheath Sn/SnO_x derived from MAX phase for microwave absorption. *J. Materiomics* **2024**, *10*, 531–542.
[46] Wang, W.; Cao, M. H. Ni_3Sn_2 alloy nanocrystals encapsulated within electrospun carbon nanofibers for enhanced microwave absorption performance. *Mater. Chem. Phys.* **2016**, *177*, 198–205.
[47] Su, J. B.; Lin, X. L.; Ma, J. C.; Shi, C. Y.; Xie, Y. N.; Xu, H. Z.; Xu, Y. Y.; Dong, X. Y.; Du, W. X.; Cao, X. Y. et al. Marangoni-driven regional salt crystallization for high salinity desalination. *Chem. Eng. J.* **2025**, *505*, 159849.
[48] Hao, B.; Chai, Z. H.; Li, M.; Duan, J. J.; Zhang, Y.; Zhang, Y. B.; Li, C. P.; Gong, C. H. Design of mesoscopic metacomposites for electromagnetic wave absorption: Enhancing performance and gaining mechanistic insights. *Soft Sci.* **2025**, *5*, 39.
[49] Ji, X. X.; Wang, H. L.; Xu, D.; Ye, X.; Chen, T. Y.; Zhao, N.; Hu, Y. L.; Xie, W.; Cao, T. S.; Tong, Y. G. Facile and scalable preparation of Ni/NiO/SiO_2@porous carbon network with strong and wide bandwidth microwave absorption. *Appl. Surf. Sci.* **2024**, *669*, 160546.
[50] Wei, B.; Zhou, J. T.; Yao, Z. J.; Haidry, A. A.; Qian, K.; Lin, H. Y.; Guo, X. L.; Chen, W. J. Excellent microwave absorption property of Nano-Ni coated hollow silicon carbide core-shell spheres. *Appl. Surf. Sci.* **2020**, *508*, 145261.
[51] Di, J. R.; Duan, Y. P.; Bo, L.; Gu, S. D.; Pang, H. F.; Jia, H. X. The Co/CoNi sequential configurations based on transparent basalt substrates toward excellent microwave absorption. *Chem. Eng. J.* **2024**, *481*, 148207.
[52] Su, J. B.; Zhang, P. K.; Yang, R.; Wang, B. L.; Zhao, H.; Wang, W. K.; Wang, C. B. MXene-based flexible and washable photothermal fabrics for efficiently continuous solar-driven evaporation and desalination of seawater. *Renew. Energy* **2022**, *195*, 407–415.
[53] Tang, J. Y.; Li, T.; Liu, Q.; Du, J. N.; Li, J. T.; Qi, Q.; Meng, F. B. Flexible microwave absorbing fabrics woven by high-strength graphene-based hybrid fibers with broadband electromagnetic response. *J. Mater. Sci. Technol.* **2024**, *200*, 93–103.
[54] Pan, F.; Cai, L.; Shi, Y. Y.; Dong, Y. Y.; Zhu, X. J.; Cheng, J.; Jiang, H. J.; Wang, X.; Zhong, S.; Lu, W. Phase engineering reinforced multiple loss network in apple tree-like liquid metal/Ni-Ni_3P/N-doped carbon fiber composites for high-performance microwave absorption. *Chem. Eng. J.* **2022**, *435*, 135009.
[55] Liu, X. X.; Xie, S. Y.; Liu, X. Y.; Yu, Z. J.; Cai, S. Y.; Tong, G. X.; Xie, L. Y.; Li, Z. Q.; Wu, W. H. Heterointerface-engineered SnO_2@SnO nanoparticle@foamed C composites for prominent microwave absorption and thermal conduction performance. *Chem. Eng. J.* **2024**, *497*, 154492.
[56] Li, S. X.; Sun, Y. J.; Jiang, X. Z.; Yu, H. Y. Spongy ternary Nano-composites with optimized impedance matching and synergistic effect for broadband and strong microwave absorption. *J. Colloid Interface Sci.* **2023**, *652*, 1197–1207.
[57] Zhang, J.; Zhang, Z. Y.; Fan, X. X.; Wang, S. J.; Kang, R. X.; Luo, J. L.; Xu, X. R.; Xiong, S. S. Elaborate design of distinctive 3D flower-like M–$Ti_3C_2T_x$@SnS@C heterostructures with structure control and surface modification as promising microwave absorbers. *Mater. Today Chem.* **2024**, *36*, 101937.
[58] Zhai, M. Z.; Zhao, S. J.; Guo, H.; Li, X. C.; Shi, X. T.; He, M. K.; Zhang, Y. L.; Gu, J. W. Bionic-structured electromagnetic interference shielding composites. *Sci. Bull.* **2025**, *70*, 2347–2364.
[59] Han, Q. Q.; Xu, J. H.; Shi, J. Y.; Zhou, M.; Wang, H. B.; Geng, L.; Xiong, J. J.; Du, Z. L. Structural and hetero-interfacial engineering of magnetic bimetallic composites based polyurethane microwave absorbing coating for marine environment. *Compos. Part A: Appl. Sci. Manuf.* **2025**, *192*, 108770.

[60] Geng, W. Z.; Liu, Y. L.; Lei, H. Y.; Song, L. M.; Wang, H. L.; Shao, G.; Zhu, Y. Q.; Zhang, R.; Min, Z. Y.; Fan, B. B. Construction of a highly ordered SiC nanofiber@C fiber heterojunction hybrid with a fuzzy grass-like structure for enhanced microwave absorbing performance. *Chem. Eng. J.* **2024**, *499*, 155785.

[61] Cai, Y. Z.; Chai, Y. L.; Cheng, L. F.; Yin, H. F.; Huang, X.; Yu, H. M.; Ren, S. X.; Chen, M. X.; Yu, Z. X.; Qiao, M. T. Directionally pressurized filtrated nitrogen-doped CNTs/RGO/carbon hollow sphere/CoNi sandwich buckypaper with superflexible, high-strength mechanical, and excellent microwave-absorbing properties. *J. Mater. Sci. Technol.* **2026**, *253*, 146–158.

[62] Woodgate, C. D.; Marchant, G. A.; Pártay, L. B.; Staunton, J. B. Structure, short-range order, and phase stability of the $Al_xCrFeCoNi$ high-entropy alloy: Insights from a perturbative, DFT-based analysis. *npj Comput. Mater.* **2024**, *10*, 271.

[63] Wang, Q.; Su, X. L.; Jia, Y.; Liu, Y.; Shahzad, F. Regulation of microstructure and absorption properties of MXene materials: Theoretical and experimental. *Adv. Sci.* **2025**, *12*, e09994.

[64] Wang, J.; Miao, Z. Q.; Gao, K. S.; Li, Z. Q.; Zhang, X. N.; Yang, C.; Iqbal, S.; Xiang, G. M.; Cui, A. G.; Liu, L. H. et al. Integration of heterogeneous interfaces and multi-dimensional encapsulation structure in Fe_2N@CNTs enabling highly efficient thermal management and microwave absorption. *Adv. Funct. Mater.* **2024**, *34*, 2408696.

[65] Liu, A.; Xu, X. S.; Qiu, H.; Guo, H.; He, M. K.; Yu, Z.; Zhang, Y. L.; Gu, J. W. Bioinspired hollow heterostructure fillers for enhanced electromagnetic interference shielding in polyimide aerogels. *InfoMat* **2025**, *7*, e70060.

[66] Guo, Y. Q.; Zhang, L.; Ruan, K. P.; Mu, Y.; He, M. K.; Gu, J. W. Enhancing hydrolysis resistance and thermal conductivity of aluminum nitride/polysiloxane composites via block copolymer-modification. *Polymer* **2025**, *323*, 128189.